7-20-2005

The Low End of the Supermassive Black Hole Mass Function: Constraining the Mass of a Nuclear Black Hole in NGC 205 via Stellar Kinematics

Monica Valluri
University of Chicago

Laura Ferrarese
Rutgers University

David Merritt
Rochester Institute of Technology

Charles L. Joseph
Rutgers University

Recommended Citation
Monica Valluri et al 2005 ApJ 628 137 https://doi.org/10.1086/430752

Accepted for Publication in The Astrophysical Journal, 20 July 2005, v628
Preprint typeset using LaTeX style emulateapj v. 6/22/04

THE LOW END OF THE SUPERMASSIVE BLACK HOLE MASS FUNCTION: CONSTRAINING THE MASS OF A NUCLEAR BLACK HOLE IN NGC 205 VIA STELLAR KINEMATICS

Monica Valluri,[1] Laura Ferrarese,[2,3] David Merritt,[4] and Charles L. Joseph[2]

Accepted for Publication in The Astrophysical Journal, 20 July 2005, v628

ABSTRACT

Hubble Space Telescope (HST) images and spectra of the nucleated dwarf elliptical galaxy NGC 205 are combined with 3-integral axisymmetric dynamical models to constrain the mass M_{BH} of a putative nuclear black hole. This is only the second attempt, after M33, to use resolved stellar kinematics to search for a nuclear black hole with mass below 10^6 solar masses. We are unable to identify a best-fit value of M_{BH} in NGC 205; however, the data impose a upper limit of $2.2\times10^4\mathrm{M}_\odot$ (1σ confidence) and and upper limit of $3.8\times10^4\mathrm{M}_\odot$ (3σ confidence). This upper limit is consistent with the extrapolation of the $M_{BH}-\sigma$ relation to the $M_{BH}<10^6\mathrm{M}_\odot$ regime. If we *assume* that NGC 205 and M33 both contain nuclear black holes, the upper limits on M_{BH} in the two galaxies imply a slope of ~ 5.5 or greater for the $M_{BH}-\sigma$ relation. We use our 3-integral models to evaluate the relaxation time and stellar collision time in NGC 205; T_r is $\sim 10^8$ yr or less in the nucleus and $T_{coll}\approx 10^{11}$ yr. The low value of T_r is consistent with core collapse having already occurred, but we are unable to draw conclusions from nuclear morphology about the presence or absence of a massive black hole.

Subject headings: galaxies: elliptical and lenticular — galaxies: structure — galaxies: nuclei — stellar dynamics

1. INTRODUCTION

Evidence for the existence of supermassive black holes (SBHs) in galactic centers has increased steadily in the past decade. Kinematical detections with varying degrees of quality have been made in roughly three dozen galaxies (see Ferrarese & Ford 2004 for a review), and virtually airtight evidence exists in two cases: our own galactic center (Ghez et al. 2003; Schödel et al. 2003) and NGC 4258 (Miyoshi et al. 1995). The measured masses obey tantalizingly tight relations with the bulge luminosity (Kormendy & Richstone 1995; McLure & Dunlop 2002; Marconi & Hunt 2003), the degree of concentration of the bulge light (Graham et al. 2001; Erwin et al. 2004), the central velocity dispersion of the stellar component (Ferrarese & Merritt 2000) and the velocity dispersion on kiloparsec (Gebhardt et al. 2000a), and the virial velocity tens-of-kiloparsec scales (Ferrarese 2002).

These relations are well established at masses exceeding $\sim 10^7\mathrm{M}_\odot$, the regime spanned by all but two of the current detections. Below $\sim 10^7\mathrm{M}_\odot$ only two measurements exist: in the Milky Way ($M_{BH}=4\times10^6$ $\mathrm{M}_\odot$, Ghez et al. 2003; Schödel et al. 2003) and in M32 ($M_{BH}=2.5\times10^6$ $\mathrm{M}_\odot$, Verolme et al. 2002, van der Marel et al. 1998). Yet extending the relations to the intermediate-mass black hole (IBH) regime ($M_{BH}\lesssim 10^6\mathrm{M}_\odot$) is crucial for constraining models of black hole formation (Haehnelt, Natarajan & Rees 1998; Cattaneo, Haehnelt & Rees 1999; Monaco, Salucci & Danese 2000; Bromley et al. 2004). For instance, the simple existence of IBHs would pose a serious challenge for models in which nuclear black holes are born *in situ* from the collapse of a "supermassive star" (e.g. Haehnelt et al. 1998). It would on the other hand, provide support for the alternative scenarios in which SBHs evolve from the migration to galactic centers of seed black holes produced, for instance, from the collapse of Population III stars, or from dynamical processes in ordinary star clusters (Gürkan, Freitag & Rasio 2004; Portegies Zwart et al. 2004; Islam, Taylor & Silk 2003, Portegies Zwart & McMillan 2002; Miller & Hamilton 2002).

Currently no fully compelling mass determinations exist in this regime. The interpretation of the superluminous off-nuclear X-ray sources (ULXs) detected in a number of nearby galaxies (Miller & Colbert 2004) is under debate. Claimed kinematical detections of IBHs in globular clusters (Gebhardt, Rich & Ho 2002; Gerssen et al. 2002) and dense star clusters (Maillard et al. 2004) have generally failed to stand up to close scrutiny (Gerssen et al. 2003; Baumgardt et al. 2003a&b; McNamara, Harrison & Anderson 2003). Although indirect evidence exists for IBHs in Seyfert galaxies (Filippenko & Ho 2003; Greene & Ho 2004), a clear dynamical detection is still lacking. In galactic nuclei, only one firm upper limit, of a few thousand solar masses, has been established for an IBH, in the late-type spiral M33 (Merritt, Ferrarese & Joseph 2001; Gebhardt et al. 2001). There is a simple reason for this rather unsatisfactory state of affairs: the dynamical influence of a $\sim 10^5\mathrm{M}_\odot$ IBH is dominant within ~ 0.3 pc (the so-called "radius of influence"), assuming that the observed scaling of nuclear properties with M_{BH} continues into the IBH regime. At optical wavelengths and at Hubble Space Telescope (HST) resolution ($\sim 0''.1$), this restricts the search to galaxies closer than ~ 1 Mpc. Several dE and dSph galaxies fit

[1] Kavli Institute for Cosmological Physics, University of Chicago, 5640 S. Ellis Avenue, Chicago 60637
valluri@oddjob.uchicago.edu
[2] Department of Physics and Astronomy, Rutgers University, New Brunswick, NJ 08854
cjoseph@physics.rutgers.edu
[3] National Research Council Canada, Herzberg Institute of Astrophysics, Victoria, BC, V9E 2E7, Canada
[4] Department of Physics, Rochester Institute of Technology, Rochester, NY 14623
merritt@astro.rit.edu

this criterion, but the need to observe objects with high enough central surface brightness leaves only one unexamined candidate: NGC 205, a dEn companion to the Andromeda galaxy. NGC 205 has been well studied from the ground (e.g. Bica et al. 1990; Carter & Sadler 1990; da Costa & Mould 1988; Lee 1996; Davidge 2003; and references therein) and in imaging mode only, with HST (Jones et al. 1996; Cappellari et al. 1999; Bertola et al. 1995). Along with M32 and the Sagittarius Dwarf (Monaco et al. 2005) it is one of the three spheroidals in the Local Group to boast a photometrically distinct nucleus (van den Bergh 1999). The dominant stellar population in the nucleus is known to have formed between 100 and 500 Myr ago, after star formation had ceased in the central region (Lee 1996). The galaxy shows no sign of nuclear activity (Ho, Filippenko & Sargent 2003; Fabbiano, Kim & Trinchieri 1992; Condon et al. 1998). Based on a measurement of the luminosity profile of the nucleus, combined with an estimate of the nuclear M/L ratio, Jones et al. (1996) estimate a mass for the nucleus of 9×10^4 $M_\odot$, which therefore sets an upper limit to the mass of any putative nuclear IBH. The relation between M_{BH} and the central stellar velocity dispersion σ predicts $M_{BH} = 7.4 \times 10^4 M_\odot$ (adopting a central velocity dispersion of $\sigma = 39 \pm 6$ km s^{-1}; Peterson & Caldwell 1993). The influence radius of such an IBH would be ~ 0.2 pc, barely resolvable by HST at the galaxy's distance of 740 kpc (Ferrarese et al. 2000).

In this paper we present new HST images and spectra of NGC 205 (§ 2); describe the modeling method and derive estimates of the mass-to-light ratios for the inner and outer regions (§ 3); construct axisymmetric dynamical models that are consistent with the kinematical data and search for a best-fit value of M_{BH} (§ 4); discuss the implications for black hole scaling relations (§ 5); and discuss the constraints that the morphology of the nucleus place on the existence of a massive black hole (§ 6). § 7 sums up.

2. OBSERVATIONS AND DATA ANALYSIS

2.1. *HST/STIS Spectra*

The nucleus of NGC 205 was observed for a total of 24,132s with the $52'' \times 0''.1$ slit of HST's Space Telescope Imaging Spectrograph (STIS) between 15 October 2002, and 22 October 2002. The Ca II absorption triplet ($\lambda\lambda$ = 8498.06, 8542.14, 8662.17 Å) was sampled with the G750M grating, covering the spectral region between 8275 Å and 8847 Å with 19.8 km s^{-1} pixel^{-1} spectral sampling (at 8500 Å). The STIS CCD pixel scale is $0''.05$, giving a spatial resolution of $0''.115$. Eleven spectra were each divided into a pair of consecutive ("CR-split") exposures to facilitate removal of cosmic rays; in addition, each spectrum was repeatedly shifted relative to the first by 2.25, 4.5 and 6.75 pixels along the dispersion direction, both to allow for correction of bad pixels and to improve the spatial resolution. The spectral calibration was performed using the IRAF task CALSTIS following the standard procedure outlined in the STIS Data Handbook (version 3.0, Mobasher, Corbin & Hsu 2001).

Correction for analog-to-digital conversion errors, bias and dark subtraction, pixel-to-pixel flat field division, 2D rectification and wavelength calibration were performed by the IRAF task CALSTIS, using the most up-to-date calibration files provided by the Space Telescope Science Institute. CALSTIS was also used to combine pairs of "CR-split" exposures, performing cosmic ray rejection in the process, and to refine the wavelength calibration using spectral lamp exposures obtained immediately before each spectrum. The latter step is necessary to correct for spectral shifts due to positioning by the Mode Select Mechanism and thermal motions. In addition, each spectrum was corrected for the "fringe" pattern which affects observations longward of 7000 Å, using flat fields obtained immediately before each spectrum, each calibrated (using the same procedure adopted for the NGC205 spectra) and normalized. Finally, all spectra were combined using the IRAF task DRIZZLE, with shifts calculated from the astrometric information recorded in the "jitter" files. The actual recorded shifts between spectra were found to be within $0''.35$ of the commanded ones, well within the positioning uncertainties of the instrument.

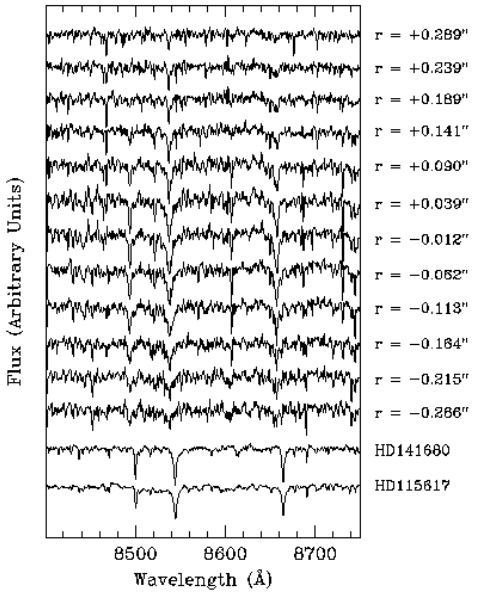

FIG. 1.— STIS spectra obtained at 12 positions along the slit. The lowest to frames show STIS spectra for the two template stars used in the analysis.

Spectra were extracted between $-0''.266$ and $+0''.289$ from the nucleus and are shown in Figure 1. At each location, the line-of-sight velocity distribution (LOSVD) was determined by deconvolving the nuclear spectra with one or more stellar templates, using the maximum penalized likelihood algorithm (Merritt 1997). Once recovered nonparametrically, the LOSVDs were represented in terms of Gauss-Hermite (GH) series (Gerhard 1993; van der Marel & Franx 1993). Confidence intervals on all quantities were computed via standard bootstrap techniques.

Recovery of the LOSVDs requires knowledge of the spectrum of a star representative of the entire stellar ensemble. In all the galaxies for which STIS stellar kinematical measurements have been obtained from stellar absorption lines (e.g. Gebhardt et al. 2003; Pinkney et al. 2003; Cappellari et al. 2002), the stellar population in the nucleus has been old enough that a single template star– generally that of the G8 III giant HD141680 – has

been adopted. Although other template stars observed with the same instrumental configuration used for the NGC 205 spectra exist in the HST archives, all but one are of late G or early type K giant stars; the exception is HD115617, a main sequence G5 star. As noted above, none of these standards is representative of the stellar population in NGC 205, raising the possibility that the kinematical parameters derived from the spectra are biased as a consequence of template mismatch. To explore this possibility, we have compared the LOSVDs derived using HD115617 (spectral type G8 III, hereafter Template 1) and HD141680 (spectral type G5 V, hereafter Template 2) as templates: their spectra are different enough (see Fig 1) to allow us to judge the effects of template mismatch on the results.

The first four terms from the Gauss-Hermite expansion, V, σ, h_3, and h_4, (van der Marel & Franx 1993; Joseph et al. 2001) derived from Template 1 and Template 2 are tabulated in Table 1 and shown in Figure 2 as crosses and filled circles respectively (the points from Template 2 have been offset slightly along the horizontal axis to allow for better visual comparison). Although the use of Template 1 resulted in a slightly better fit to the NGC205 spectrum (as measured via the integrated square error), the V and σ values from both templates are identical to within 1σ statistical errors. The overall consistency in the h_3 and h_4 terms is also quite good: all values are consistent with zero.

The largest discrepancy is seen in the shape of the central ($r = -0''.012$) LOSVD, shown in Figure 3; this is particularly relevant since it is on the central LOSVD that a black hole (if present) is expected to have the strongest effect. The noticable asymmetry in the central LOSVD obtained when using Template 1 (solid line) is absent when Template 2 is used instead (dot-dash line). In an axisymmetric galaxy, strong asymmetries in the central LOSVD are unphysical, and the asymmetry recovered with Template 1 is therefore very likely the spurious result of template mismatch.

In summary, the consistency in the V, σ, h_3, and h_4 parameters derived using the two different templates gives us some degree of confidence that template mismatch is unlikely to significantly affect our results, although we should treat results which make use of the full central LOSVD with caution. We further note that for stellar types earlier than F stars, temperature and rotation increase the intrinsic width of the lines, and the presence of hydrogen absorption lines from the Paschen series can further complicate matters as they can overlap with the calcium features. In general, using an old stellar template to measure the kinematics of a young stellar population in this spectral region will cause the velocity dispersion, and therefore M_{BH}, to be *overestimated*. Since only an upper limit to M_{BH} will be derived in the following sections, we conclude that the upper limit could only *decrease* if the correct stellar template were used. In other words, the value derived below should be considered as a very firm upper limit to the mass of a central IBH in NGC 205.

Finally, STIS data were complemented at large radii with the ground-based kinematic data from Bender, Paquet & Nieto (1991), obtained with the 3.5m telescope at Calar Alto, consisting of 31 apertures within $84.56''$.

2.2. *HST/ACS Images*

In order to determine the luminosity distribution in NGC 205, the galaxy was observed on 03 October 2002 for a total of 2,440s with the F814W filter ($\sim$ Johnsons' I) of the Advanced Camera for Surveys (ACS) High Resolution Channel (HRC). The HRC pixel scale is $0''.027$, giving a field of view of $29''\times26''$. To improve the spatial resolution, NGC 205 was observed at four different pointings, each consisting of two CR-split images, arranged at the corners of a square of side $0''.0989$. Total exposure times were 2,560s in F555W and 2,440s in F814W. Image calibration was performed using the IRAF tasks CALACS and PYDRIZZLE following the standard procedure described in the ACS Data Handbook (Mobasher, Corbin, & Hsu 2003). Basic reduction (bias and dark subtraction, removal of overscan regions, flat fielding and cosmic ray removal) was performed using IRAF's CALACS, while the task PYDRIZZLE was used to correct for geometric distortion, and combine the four drizzled images.

The structural parameters of NGC205 will be discussed in detail in a forthcoming paper. Briefly, two independent procedures were adopted to recover the isophotal parameters. The IRAF task ELLIPSE (Jedrzejewski 1987) was employed to find the best fitting isophotes by iteratively sampling the image along elliptical paths with given semi-major axis length, keeping as free parameters the position of the center, ellipticity, semi-major axis position angle, and high order coefficients describing deviations of the isophotes from ellipses. ELLIPSE is best applied to galaxies with a smooth surface brightness distribution; in the case of NGC 205, the task fails to converge beyond $0''.8$, where the stellar population is clearly resolved. Fischer et al. (1992) introduced a different approach, in which the image is divided in ellipsoidal annuli, each further divided into eight sectors. The median of the average brightnesses determined in each sector is taken as the average brightness of each annulus. In the case of NGC 205, the center and ellipticity of each annulus was set equal to the center found by ELLIPSE within $0''.8$, and the average ellipticity measured by Kim & Lee (1998) and Lee (1996) from ground based data respectively.

The photometric calibration was performed using the zero points from Sirianni et al. (2004) and a foreground extinction correction $E(B-V) = 0.081$ (Schlegel, Finkbeiner & Davis 1998), giving $A(I) = 0.151$ for $R_V = A(V)/E(B-V) = 3.1$ and $A(I)/A(V) = 0.594$ (Cardelli, Clayton & Mathis 1989). The resulting surface brightness profile is shown in Figure 4, where we also plot the $I-$band surface brightness profiles measured from ground-based data by Kim & Lee (1998) and Lee (1996). The ACS surface brightness profiles determined using the two methods described above are in excellent agreement. Both agree with the ground-based profiles except in the innermost $\sim 1''$, where the latter are strongly affected by seeing. The final, combined, composite $I-$band surface brightess profile is tabulated in Table 2.

The 3-dimensional luminosity density $j_*(\varpi, z)$ was computed via a non-parametric algorithm (Merritt, Meylan & Mayor 1997) under the assumption that the galaxy is seen edge-on. The inner radius of the surface brightness distribution $0''.025$ and the outer radius of the sur-

TABLE 1
HST/STIS Kinematics for the Nucleus of NGC 205

r	Template HD141680								Template HD115617							
	V	ΔV	σ	$\Delta\sigma$	h_3	Δh_3	h_4	Δh_4	V	ΔV	σ	$\Delta\sigma$	h_3	Δh_3	h_4	Δh_4
(1)	(2)	(3)	(4)	(5)	(6)	(7)	(8)	(9)	(10)	(11)	(12)	(13)	(14)	(15)	(16)	(17) [1]
-0.266	4.62	7.45	17.04	5.65	-0.13	0.13	0.06	0.05	0.47	6.75	21.90	6.20	0.01	0.07	0.00	0.04
-0.215	9.97	5.80	22.12	7.05	-0.14	0.15	0.05	0.04	13.23	6.60	28.16	7.80	0.00	0.10	-0.02	0.06
-0.164	-1.62	4.30	15.75	3.55	0.05	0.09	0.05	0.03	-1.09	3.95	17.59	2.80	0.08	0.03	0.05	0.02
-0.113	-5.87	4.00	15.39	4.45	0.03	0.05	0.06	0.03	-5.02	3.65	16.87	1.75	0.07	0.02	0.04	0.01
-0.062	-4.50	4.05	18.14	4.65	0.00	0.06	0.09	0.04	-5.57	3.85	19.46	2.80	0.08	0.02	0.04	0.01
-0.012	-0.40	4.30	20.55	4.00	0.03	0.07	0.09	0.03	-0.62	3.95	21.41	3.35	0.05	0.06	0.03	0.02
0.039	0.10	3.60	16.20	2.95	0.06	0.08	0.04	0.02	2.85	2.80	15.93	1.95	0.01	0.02	0.00	0.00
0.090	-3.19	4.00	16.60	3.55	0.05	0.08	0.06	0.03	-0.12	3.70	18.52	3.55	0.08	0.05	0.04	0.03
0.141	-4.12	5.00	17.69	4.85	0.03	0.07	0.08	0.04	0.97	5.25	19.62	4.55	0.06	0.06	0.04	0.03
0.189	-3.97	4.95	15.61	5.20	-0.10	0.07	0.06	0.04	-0.72	6.35	19.60	5.20	-0.11	0.10	0.07	0.06
0.239	-0.19	5.70	11.73	2.80	-0.04	0.04	0.03	0.02	0.91	5.35	13.22	2.05	0.00	0.03	0.01	0.01
0.289	-1.85	6.00	10.18	3.45	-0.02	0.05	0.02	0.02	1.64	5.05	11.57	1.35	0.00	0.01	0.01	0.00

[1]Columns are: (1) Aperture distance from the morphological center of NGC 205; (2, 10) velocity (in km s^{-1}) relative to the heliocentric velocity of NGC205 (-241km s^{-1}); (3, 11) 1σ error on V; (4, 12
14) C
Gaus

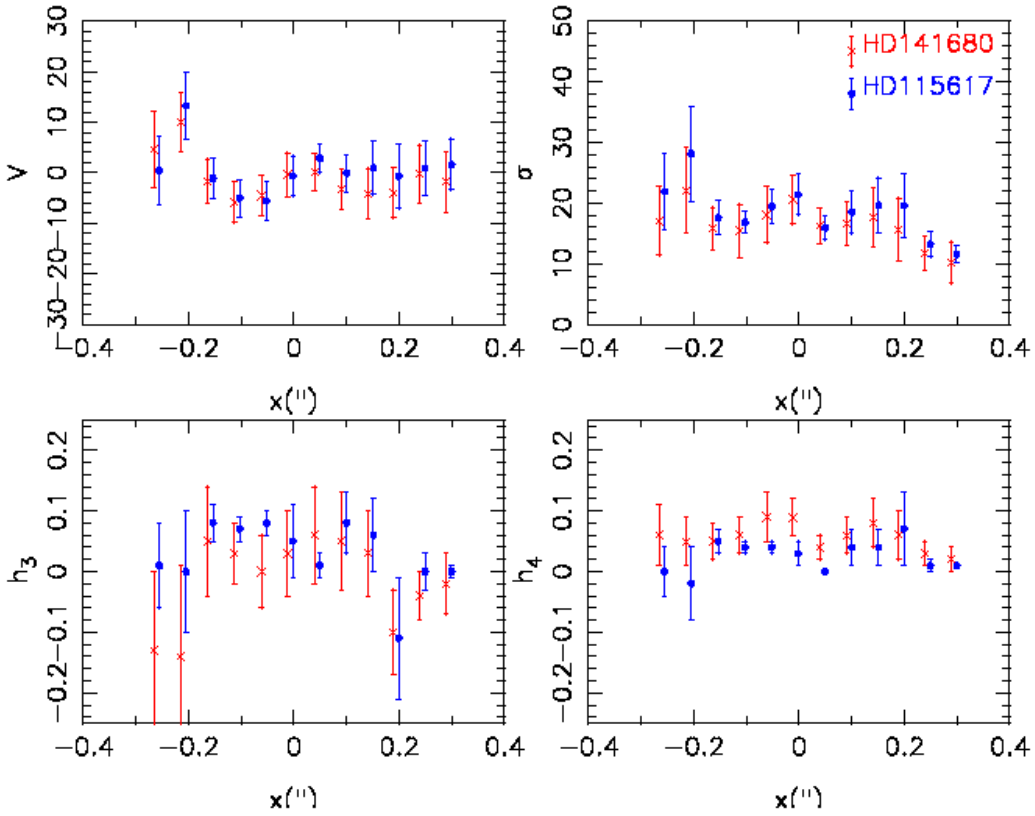

Fig. 2.— Nuclear kinematical data (V, σ, h_3, h_4) along the slit obtained by deconvolving STIS spectra (Fig 1) with two different stellar templates HD141680 (crosses) HD115617 (filled circles - which have been offset slightly along the horizontal axis by an arbitrary amount to enhance visibility.)

face brightness distribution is 100″. The deprojection is performed on a 2D logarithmically spaced grid with 100 grid points in each dimension. The algorithm accounts for the varying ellipticity as a function of radius and computes $j_*(\varpi, z)$ on the 2D grid by minimizing the residuals between the projected j_* and the observed surface brightness. Since the deprojection is an unstable process, smoothness was enforced via a "thin-plate smoothing spline" penalty function (Wahba 1990).

3. DYNAMICAL MODELING

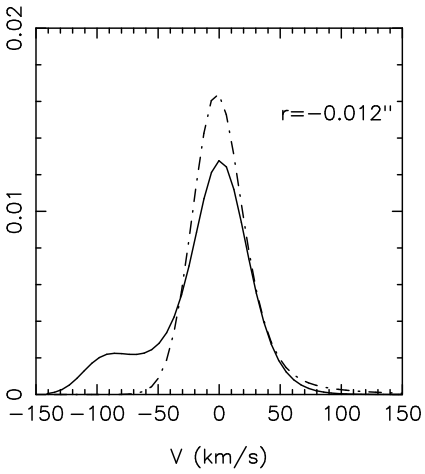

FIG. 3.— LOSVD in STIS aperture closest to the center ($r = -0''.012$) obtained with the two different stellar templates. Solid curve corresponds to deconvolution with Template 1 (a G8 III star) and dot-dash curve corresponds to deconvolution with Template 2 (a G5 III star). The velocity is with respect to the heliocentric velocity of the galaxy. The vertical axis is in arbitrary units.

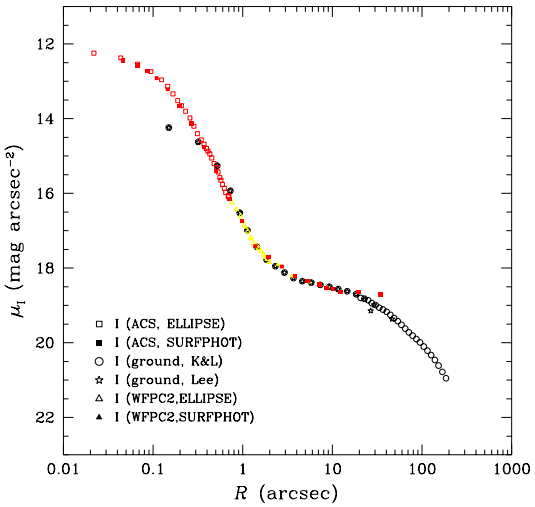

FIG. 4.— The $I-$band surface brightness profile of NGC 205, obtained by combining the HST/ACS observation discussed in this paper to the ground-based data of Kim & Lee (1998) and Lee (1996). The radius is the "effective radius", given by $r = r_{SMA}\sqrt{1-\epsilon(r)}$, where r_{SMA} is the galaxy semi-major axis, and ϵ the ellipticity.

TABLE 2
COMPOSITE $I-$BAND SURFACE BRIGHTNESS PROFILE FOR NGC 205

r (1)	I (2)	ϵ (3)	r (1)	I (2)	ϵ (3)[1]
0.025	12.35	0.2286	17.53	18.62	0.52
0.05	12.48	0.234	22.91	18.7	0.29
0.075	12.65	0.1953	24.29	18.8	0.27
0.1	12.85	0.0988	27.09	18.82	0.29
0.125	13.07	0.0082	30.01	18.86	0.3
0.15	13.24	0.0566	33.01	18.94	0.31
0.175	13.44	0.0891	37.12	18.99	0.33
0.2	13.62	0.1132	41.45	19.06	0.34
0.225	13.76	0.1453	44.91	19.11	0.35
0.25	13.91	0.1449	50.16	19.17	0.34
0.275	14.09	0.1177	55.6	19.25	0.36
0.3	14.31	0.0909	61.16	19.34	0.36
0.325	14.51	0.0718	68.35	19.42	0.38
0.35	14.67	0.0234	76.43	19.52	0.4
0.3855	14.85	0.091	85.51	19.62	0.42
0.5328	15.5	0.091	95.72	19.72	0.43
0.7418	16.24	0.091	106.3	19.81	0.45
1.037	16.82	0.091	118.0	19.9	0.46
1.454	17.47	0.091	129.8	19.99	0.46
2.043	17.76	0.091	144.1	20.1	0.47
2.876	17.99	0.091	158.5	20.21	0.47
4.051	18.24	0.091	179.5	20.33	0.5
5.605	18.36	0.091	197.4	20.46	0.5
7.543	18.43	0.091	217.2	20.61	0.5
9.157	18.51	0.091	238.9	20.78	0.5
13.92	18.56	0.3	262.8	20.95	0.5

[1]Columns are: (1) Semi-major axis length (in arcsec); (2) $I-$band magnitude; (3) Ellipticity. Data for $r \leq 0''.35$ are derived by applying IRAF/ELLIPSE to the ACS/HRC data. Data for $0''.3855 \leq r \leq 9''.157$ are measured using the radial annuli technique described in § 2, again from the HRC images. Data at larger radii are based on ground-based data from Kim & Lee (1998)

Dynamical constraints on the possible values of the parameters, the black hole mass M_{BH} and the stellar M/L ratio Υ, were computed via orbital superposition (Schwarzschild 1979) by constructing oblate spheroidal models for a large number of $[M_{BH}, \Upsilon]$. The observable properties of the models were then compared to the surface brightness and spectral data. With the exceptions detailed in §3.1 and §3.2, the modeling algorithm used is the one described in Valluri et al. (2004, hereafter VME04), to which paper we refer the reader for a detailed description of the method. The numerically-computed orbits were "observed" at each of the 31 ground-based apertures and the 12 STIS apertures. For the STIS apertures, a Gaussian PSF with FWHM of $0''.1$ was assumed (Bower et al. 2001), and the model results degraded accordingly. Detailed seeing information is not available for the ground-based data, therefore the corresponding model results were not PSF-convolved. We have found that the omission is unimportant as long as the data were obtained with apertures wider than the seeing disk, which is indeed the case for the ground-based observations used in the analysis.

A non-negative quadratic programming routine (E04NCF of the NAG libraries) was used to find the weighted superposition of the orbits that best reproduces both the assumed model stellar density distribution $\rho(\varpi, z)$ and the observed kinematical data. The total number of luminosity constraints in NGC 205 is 304 (of which the inner 128 are from the ACS photometry); kinematical constraints consist of 62 contraints from the ground-based data (velocities V and velocity dispersions σ within $84''.56$) and 40 contraints from the STIS data (V, σ and the GH moments h_3, h_4) (Note: the last two apertures on the right end of the slit in Fig 2 were accidentally excluded from the dataset).

Since it is necessary to explore a wide range of the parameters values: M_{BH}, M/L-ratio (typically between 150-200 pairs of parameters), we run an intitial set of models using a total of 4500 orbits per model. Since the solution space is sensitive to the size of the orbit library (see VME04), we follow these initial runs with a limited number of models (keeping either M_{BH} or M/L-ratio fixed) with larger libraries of 8100 orbits each. The

CPU time required for a single model with 8100 orbits is 7.5 hours on a 2.4GHz Intel Xeon processor makes it prohibitively expensive to run a large number of models at this resolution). In the next two subsections we discuss two aspects in which our models differ from those described in VME04.

3.1. *Radially Varying Mass to Light Ratios*

In the standard treatment of the 3-integral modeling problem the luminosity density - derived as described in §2.2 - is converted into a mass density via a mass-to-light ratio Υ, $\rho_*(\varpi, z) = \Upsilon j_*(\varpi, z)$. In most studies, Υ is assumed to be constant over the entire galaxy. Under this standard assumption, our initial models were unable to produce an even remotely reasonable fit to the kinematics in NGC 205. This is not surprising since Υ is known to show significant radial variations in this galaxy. For instance, Carter & Sadler (1990), using simple King models, find $\Upsilon_R = 9.4$ for the main body of the galaxy (with an uncertainty of up to a factor of 2, especially at large radii) and $\Upsilon_R = 2.35$ for the nucleus (equivalent to I-band values of $\Upsilon_I = 6.95$ and $\Upsilon_I = 1.94$ respectively using standard color corrections). Allowing for a radial change in Υ mandates a cautionary note: the problem of determining both M_{BH} and $\Upsilon(r)$ is likely to be degenerate, and in principle a variety of possible Υ profiles could undoubtedly be found that fit the observational constraints equally well, each producing a different best-fit (or upper limit) value for M_{BH}.

We produced an independent estimate of Υ_I in NGC 205 by using the 3-integral models to fit the luminosity distributions and the kinematical data separately for the nucleus and the main body of the galaxy. The luminosity density of the nucleus is well approximated by a Gaussian with FWHM $\sim 0''.26$ (or $\sigma = 0''.11$) and the nucleus can therefore be regarded as the region within $r \leq 0''.33$ (corresponding to $\sim 3\sigma$ of the Gaussian fit to the luminosity density of the nucleus). The main body can be regarded as the region beyond $r \geq 0''.55$ ($\sim 5\sigma$ of the Gaussian fit to the luminosity density of the nucleus) where the color and luminosity profile change over to that of the main body of the galaxy. Figure 5 shows 1D curves of $\Delta\chi^2 = \chi^2 - \chi^2_{min}$ for the nucleus alone ($r \leq 0''.33$, solid line) and for the outer region alone ($r \geq 0''.55$, red dot-dash line) as a function of Υ_I for the case in which no black hole is present. All models used a library with 8100 orbits. The horizontal thin dot-dash line is at $\Delta\chi^2 = 1$. The solid black line suggests that $(\Upsilon_I)_{nucleus} = 1.6 \pm 0.8$ (1σ uncertainties) and $(\Upsilon_I)_{body} = 9 \pm^{1.3}_{2.5}$, consistent within 1σ with the values derived by Carter & Sadler (1990). We point out that neither estimate is flawless. The adoption of King profiles is not motivated by current data (or our current knowledge of the power law form of luminosity profiles of elliptical galaxies). Currently both methods assume that it is possible to estimate M/L ratios separately for the two regions by treating them as dynamically separate. However in practice they are a single dynamical entity and the M/L profile needs to be obtained for both regions simultaneously. The most general method for finding the radial profile$\Upsilon_I(r)$ would be to allow M/L to vary with radius and obtain a non-parametric best-fit estimate for this function for this using a method similar to the Schwarzschild method. This beyond the scope of the current paper.

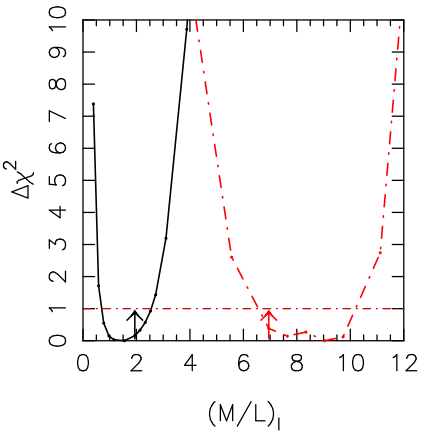

FIG. 5.— 1D curves of $\Delta\chi^2$ for the nuclear region ($r \leq 0''.33$, solid line) and for the main body of the galaxy ($r \geq 0''.6$, red dot-dash line) as a function of the I-Band M/L ratio Υ_I. All models assume $M_{BH} = 0$ and used 8100 orbits each. The vertical arrows show the Υ_I values obtained by Sadler and Carter (1990) using King-models.

For lack of stronger constraints, we make the simplest possible assumption about the radial variation of Υ, namely we assume Υ_I to be constant within $0''.33$ (the nuclear region) and beyond $0''.55$ (the main body of the galaxy), and to vary linearly between these two values at intermediate radii. Although the values of Υ derived by Carter & Sadler and those derived using the Schwarzschild method are consistent, in the following section we will carry out the dynamical modeling using both. In the first case (the "Carter-Sadler profile") we adopt $\Upsilon_I = 1.94$ for $r \leq 0''.33$, $\Upsilon_I = 6.95$ for $r \geq 0''.55$ and linearly-varying between these two radii. In the second case (the "Schwarzschild profile") we adopt $\Upsilon_I = 1.6$ for $r \leq 0''.33$, $\Upsilon_I = 8.5$ for $r \geq 0''.55$ and linearly-varying in between. In what follows we will indicate these "primary" profiles as $\Upsilon^*_I(r)$, and introduce, in the dynamical modeling, a scaling factor, $S_\Upsilon = \Upsilon_I(r)/\Upsilon^*_I(r)$, as a free parameter. The second free parameter is the mass M_{BH} of the central black hole. For libraries which adopted the Carter-Sadler Υ-profile we constructed dynamical models for 17 different values of M_{BH} in the range $0 \leq M_{BH} \leq 10^7 M_\odot$ and ~ 13 values of S_Υ. For libraries which adopted the Schwarzschild Υ-profile we constructed dynamical models for 15 different values of M_{BH} in the range $0 \leq M_{BH} \leq 10^6$ $M_\odot$ and 13 values of S_Υ.

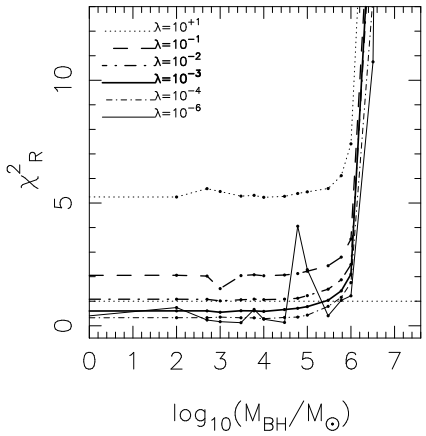

FIG. 6.— 1D reduced χ^2 (χ^2_R) curves as a function of black hole mass (M_{BH}) for 6 different values of the regularization (smoothing) parameter λ. All models assume $\Upsilon_I = 1.1$. See text for further details.

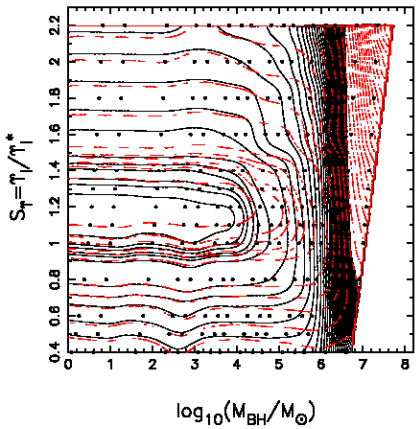

FIG. 7.— Contours of constant χ^2 derived from fits of the data to 3-Integral axisymmetric models. Dashed contours: fits to the Bender et al. (1991) ground-based data. Solid contours: fit to the combined ground-based + STIS GH moments derived using Template 1. Each dot represents a set of parameters (M_{BH}, S_Υ) for which a 3-Integral dynamical model was constructed. The total number of orbits used in each case was $N_o = 4500$. The first 3 contours of each type are at $1\sigma, 2\sigma, 3\sigma$ confidence intervals respectively (68.5%, 90% and 95%). The regularization parameter was $\lambda = 10^{-3}$.

3.2. *Regularization*

It is customary to smooth, or "regularize", the orbital solutions, either by including a penalty function with adjustable smoothing parameter (e.g. VME04), by imposing a "maximum entropy" constraint (e.g. Gebhardt et al. 2003) or by imposing a local smoothness constraint in phase space (Cretton et al. 1999). As discussed at length in VME04, the results can depend strongly on the value of the smoothing parameter λ. An incorrectly chosen λ can generate misleading results; for instance, too great a degree of smoothing has the same effect as limiting the range of allowed orbital populations, and can give a spurious, best-fit value of M_{BH} even when no value is preferred by the data. Since the optimal choice of λ depends on the data set in question, we constructed models for nine different values of λ between 10^{-7} and 10. In the interest of time, all models used the Carter-Sadler Υ-profiles and libraries of 4500 orbits.

1D reduced χ^2 curves (χ^2_R) for a fixed $S_\Upsilon = 1.1$ (the Υ-scaling factor defined in § 3.1) are plotted in Figure 6 for six values of λ. (χ^2_R is computed for DOF=100 as discussed later in § refsec:carter-sadler). Most of the curves are characterized by a nearly flat valley in χ^2 at $M_{BH} < 10^5 M_\odot$. Figure 6 also shows that for smallest value of $\lambda = 10^{-6}$ (thin solid curve) the χ^2_R plot is noisy and oscillates randomly from one model to the next. For $\lambda = 10^{-4} - 10^{-2}$ the curves are qualitatively similar: flat from $M_{BH} = 0 - 10^5 M_\odot$ followed by a sharp upturn at higher M_{BH}. For $\lambda = 10^{-4}$ the $\chi^2_R = 0.23$ in the flat region, for 10^{-3} the $\chi^2_R = 0.62$ in the flat region (thick solid line) and for $\lambda = 10^{-2}$ the $\chi^2_R = 1.07$. For values of λ larger than $\lambda = 10^{-2}$ χ^2_R increases above one, and the upper limit on M_{BH} depends more sensitively on λ, with M_{BH} decreasing as λ increases. We could choose either $\lambda = 10^{-3}$ or $\lambda = 10^{-2}$. We chose $\lambda = 10^{-3}$ as the value that gives the largest $\chi^2_R < 1$. In the remainder of this paper (unless otherwise noted) this is our preferred value of $\lambda = 10^{-3}$. Other, ostensibly, "objective" methods to determine the optimal value of the regularization parameter exist but they are either not well motivated physically or extremely costly computationally. In the interest of limiting the number of parameters varied we use of $\lambda = 10^{-3}$ also for models using libraries of 8100 orbits. Our quoted results of the upper limit on M_{BH} and choice of S_Υ are all for this value of λ, but this does not imply that other values of λ give statistically less probable results.

4. RESULTS OF 3-INTEGRAL MODELING

4.1. *The Zeroth-Order Model*

We begin our analysis by discussing the results of the dynamical models under the following conditions: 1) all models use a 4500 orbit library; 2) the regularization parameter λ is set equal to 10^{-3}; 3) the Υ^*_I profile is that given by Carter and Sadler (1990) (§3.1); and 4) the STIS kinematical information is extracted using Template 1 (§2.1). In the next subsection we will change some of these conditions and investigate how the results are affected.

Figure 7 shows 2-dimensional contour plots of the total χ^2 as a function of $S_\Upsilon = \Upsilon_I(r)/\Upsilon^*_I(r)$ and M_{BH}. The models covered 17 values of M_{BH} and 13 values of S_Υ (indicated by the grid of points); the contours are plotted at $\Delta(\chi^2) = 2.30, 4.61, 6.17, 9.21, 11.8, 18.4$ which correspond to 68.3%, 90%, 95.4%, 99%, 99.73%, 99.99% confidence intervals assuming two degrees of freedom (DOF) (but see note below). Beyond the 6th contour the spacing of contours is arbitrary. Two sets of contours are shown, depending on which set of kinematical constraints are fitted. While every model is required to fit the luminosity (mass) constraints (for a total of 304 constraints), the dashed (red) contours correspond to models which were required to fit the ground-based kinematical data only (a total of 62 constraints). The solid (black) contours show the results when the fit is also required to be constrained by the STIS data (V, σ, h_3 and h_4) for an additional 40 constraints.

Both sets of χ^2 contours are striking in their lack of dependence on S_Υ, which is determined from these plots to be $1.13 \pm^{0.08}_{0.1}$ (1σ uncertainty). Although a minimum

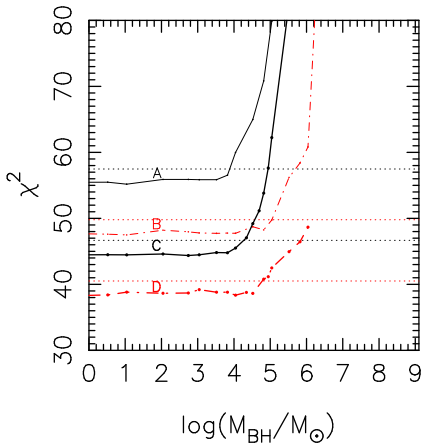

FIG. 8.— 1D χ^2 curves which illustrate the dependence of the upper limit on M_{BH} on orbit library size and on smoothing parameter λ. Individual curves are described in the text.

TABLE 3
RESULTS OF THE DYNAMICAL MODELING

Run No.	No. Orbits	λ	Υ_I[1]	Template	Constraints[2]	S_Υ	M_{BH} ($M_\odot$)
1	4500	10^{-3}	CS	1	G	$1.13\pm^{0.08}_{0.1}$	$< 1\times10^5$
2	4500	10^{-3}	CS	1	G-Sgh	$1.13\pm^{0.08}_{0.1}$	$< 8\times10^3$
3	8100	10^{-3}	CS	1	G	fixed at 1.1	$< 6.4\times10^4$
4	8100	10^{-3}	CS	1	G-Sgh	fixed at 1.1	$< 2.2\times10^4$
5	8100	10^{-4}	CS	1	G-Sgh	fixed at 1.1	$< 3.5\times10^4$
6	8100	10^{-2}	CS	1	G-Sgh	fixed at 1.1	$< 1.1\times10^4$
7	8100	10^{-1}	CS	1	G-Sgh	fixed at 1.1	$< 0.8\times10^4$
8	4500	10^{-3}	CS	2	G-Sgh	$1.13\pm^{0.08}_{0.1}$	$< 8\times10^3$
9	8100	10^{-3}	CS	1	G-Slos-Sgh	fixed at 1.1	$< 2.2\times10^4$
10	8100	10^{-3}	CS	2	G-Slos-Sgh	fixed at 1.1	$< 2.2\times10^4$
11	4500	10^{-3}	S	1	G-Sgh	$0.95\pm^{0.05}_{0.08}$	$< 1.0\times10^4$
12	8100	10^{-3}	S	1	G-Sgh	fixed at 1.0	$< 1.3\times10^4$

[1]Carter-Sadler Υ profile (CS) or Schwarzschild Υ profile (S)
[2]Ground-based data only (G); Ground+STIS GH-moments (G-Sgh); Ground+STIS Central LOSVD +STIS GH for other apertures (G-Slos-Sgh)

in the χ^2 contours is not seen, the addition of the small-radius spectral data from STIS allows us to reduce the upper limit on M_{BH} *by an order of magnitude*, as shown more clearly in Figure 8. The curves labeled **A, B** are 1D cuts through Figure 7 at the minimum in $S_\Upsilon = 1.1$: curve **A** is a fit to the ground and STIS data and gives an upper limit of $M_{BH} \approx 8\times10^3 M_\odot$ while curve **B** is the fit to the ground-based data alone and gives an upper limit of $M_{BH} \approx 10^5 M_\odot$ (both upper limits are given at the 1σ confidence level, shown by the the horizontal dotted lines drawn above each χ^2 curve). Note that the 1D χ^2 plots shown in Figure 8 *are not marginalized* with respect to S_Υ, but are merely cuts through the 2-parameter χ^2 plots. (Curves **C** and **D** of Fig8 are described in the following section.)

A well known assumption of the use of the χ^2 statistic is that the problem is linear in the parameters being estimated. An additional unstated assumption in all discussions of confidence interval estimation (e.g. Press et al. 1992) is that the number of fitted parameters is less than the number of data points – in other words, that the parameter estimation problem is over-constrained by the data. It is only in this case that quantities like "number of degrees of freedom" (DOF=$N_{\rm data} - N_{\rm parameters}$) make any sense. But in Schwarzschild modeling, the number of parameters (orbits + potential parameters) is typically far greater than the number of data points, i.e., the problem is under-constrained by the data.Indeed, one typically finds that a variety of choices for the parameters (M_{BH}, Υ) can reproduce the data equally well (VME04), and if it were not for positivity constraints on the orbital occupation numbers, this degeneracy would be even greater. We know of no discussion in the statistical literature that deals adequately with this situation, and for this reason, the standard prescriptions for estimating confidence regions (e.g. Press et al.) should be considered suspect when applied to Schwarzschild modelling.

It is therefore necessary to for us to first clarify how the confidence intervals are computed. The quality of a particular fit was assessed by comparing the total χ^2 value of the fit to the number of degrees of freedom (DOF), as being "the number of independent data points - number of *potential* parameters". Thus the number of parameters is assumed to be 2 (while actually it is much larger due to the orbits). For the NGC 205 dataset, the number of independent data points is 102 (for the STIS plus ground-based kinematical data) or 62 (for the ground-based kinematical data only; note that the luminosity constraints are "model constraints" and not "data constraints"), while the number of parameters is two (S_Υ and M_{BH}), giving DOF=100 (STIS+ground based data) or DOF=60 (ground-based data only). This DOF was used in § 3.2 to compute reduced-χ^2 (χ^2_R) which is expected to be ~ 1 for a good fit. It has become customary in this field to further assume that the confidence intervals on the parameters being estimated (namely M_{BH} and Υ) can be obtained from $\Delta(\chi^2)$ distribution with the number of degrees of freedom = to the number of parameters.

Note also that unless otherwise stated the upper limits quoted are 1σ confidence limits. In a few instances we also quote 3σ limits. Also we caution that the contour plots are *not* reliable for determining upperlimits since they are plotted with an algorithm which uses adaptive 2D regression - we always compute upperlimits from 1D cuts through the χ^2 plots. It is also worth noting that when judging whether, for instance, a model with a black hole is preferred over a black-hole-free model, we urge the skeptical reader to follow our practice of closely inspecting the kinematical profiles predicted by the different models and deciding whether either model is significantly better at reproducing the data in the region where the black hole's influence would be felt.

4.2. *Robustness of the Results*

In this section we explore the dependence of the results obtained above on 1) the size of the orbit library; 2) the choice of the smoothing parameter λ; 3) the stellar template used in recovering the kinematical data from the STIS spectra; and 4) the choice of Υ profile. The results of all models discussed in this section are summarized in Table 3.

We consider first the size of the orbit library. Curves

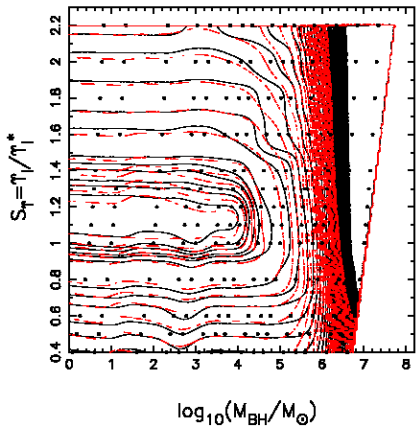

FIG. 9.— Comparison of χ^2 contours for models that fit the STIS GH moments obtained using the two different stellar templates. Solid (black) contours are for models that fit kinematics derived using Template 1 and dot-dash (red) contours are for models that fit kinematics from Template 2.

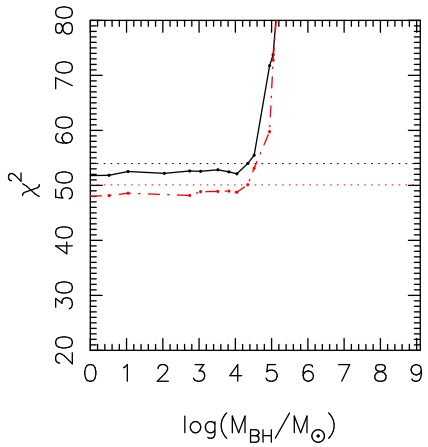

FIG. 10.— 1D-χ^2 curves obtained by fitting the central LOSVD and the Gauss-Hermite moments for other apertures. The solid line is from fitting the central LOSVD and GH moments for other apertures obtained with Template 1 and the dot-dash line is from fitting the kinematics obtained with Template 2.

C, D in Figure 8 are analogous to curves **A, B** except they were derived from models which used 8100 orbits. In the interest of time, these models were run at $\Upsilon_I(r)/\Upsilon_I^*(r) = 1.1$, for 17 different values of M_{BH}. It is evident from the figure that increasing the size of the orbit library relaxes the upper limit on M_{BH}, at least when both the STIS and ground based data are fitted. Using the ground based-data only, we now derive an upper limit of $M_{BH} = 6.4 \times 10^4 M_\odot$ (curve **D**), while adding the STIS constraints produces an upper limit $M_{BH} \lesssim 2.2 \times 10^4 M_\odot$ (curve **C**) (at 1σ confidence) and an upper limit of $M_{BH} \lesssim 3.9 \times 10^4 M_\odot$ (at 3σ confidence). This sensitivity to the size of the orbit library was discussed in VME04, where we advocated using the largest orbit library that was computationally feasible to obtain the full range of statistically allowed solutions. (We do not believe that the decrease in upper limit of M_{BH} derived from the ground-based data is statistically significant. An examination of the contribution to χ^2 shows that this number is sensitive to the the noise in the large radius data which has no bearing on the mass of a central black hole.)

As mentioned earlier, the choice of λ depends on the size of the orbit library. For the 4500 orbit models, $\lambda = 10^{-3}$ was identified in §3.2 as the best value based on the fact that this gave a χ^2_R closest to, but below one. The effect of changing λ for this larger orbit library is shown Table 3 (Run No. 4-7). When the full dataset (STIS+ground based) is fitted with a smaller smoothing parameter $\lambda = 10^{-4}$, the 1σ upperlimit increases by 60% to $M_{BH} \lesssim 3.5 \times 10^4 M_\odot$ (with $\chi^2_R \sim 0.23$. When the same dataset is fitted with a larger smoothing parameter $\lambda = 10^{-2}$, the upperlimit deccreases by 50% to $M_{BH} \lesssim 1.1 \times 10^4 M_\odot$ (with $\chi^2_R \sim 0.9$. And when the dataset is fitted with $\lambda = 10^{-1}$, the upperlimit decreases even further to $M_{BH} \lesssim 0.77 \times 10^4 M_\odot$ (with reduced $\chi^2 \sim 1.4$.

As λ increases, the fit to the data becomes smoother and as a consequence χ^2 also increases. We know of no truly robust way to pick smoothing such that it does not strongly influence the derived estimate of M_{BH}. In the absence of a robust choice of λ we simply quote the value obtained for $\lambda = 10^{-3}$ for reasons given in § 3.2.

The effect of using a different template in extracting the kinematical constraints from the STIS data (§2.1) is shown in Figure 9. This figure is directly comparable to Figure 7, since it was produced using a 4500 orbit library and $\lambda = 10^{-3}$. As expected based on the consistency between the V, σ, h_3, h_4 values shown in Figure 2, the fits to the kinematics using the two stellar templates give virtually identical limits on both S_Υ and M_{BH}.

However, as discussed in §2.1 and shown in Figure 3, the two different templates do produce significantly different shapes for the LOSVD in the innermost apertures. While these differences are disconcerting, it is nevertheless desirable to try to include the extra information contained within the central LOSVD, since it is here that the effect of a central black hole would make its presence most strongly felt (e.g. van der Marel 1994). Earlier authors (e.g. Gebhardt et al. 2000b) have modeled even strongly asymmetric central LOSVDs in the detection of a nuclear black hole with axisymmetric models. These authors attribute the asymmetry in the central LOSVD to an off-centered central aperture as well as due to the presence of obscuring dust.

Figure 10 shows two 1D-χ^2 plots obtained by fitting the full LOSVD (sampled at $\Delta V = 20$km s^{-1}) for the central STIS aperture, and the Gauss-Hermite moments for other apertures. The solid and dot-dashed lines refer to fits to the kinematics derived using Template 1 and Template 2 respectively; as before, the two horizontal dot-dash lines represent the 1σ confidence limit above the minimum of the corresponding curve. All models used orbit libraries with 8100 orbits and a smoothing parameter $\lambda = 10^{-3}$. Although the models that fit kinematics from Template 1 (solid line black) give a systematically higher χ^2 because of the difficulty in fitting the highly asymmetric central LOSVD, both LOSVDs produce identical upper limits on M_{BH} of $2.2 \times 10^4 M_\odot$ - which is also identical to that obtained from fitting the GH moments for all the apertures (curve **C** in Fig 7). The insensitivity of the results to whether the full LOSVD is fitted or not, is likely to be a result of the fact that the sphere of influence of a putative central black hole in NGC 205 is not resolved, and therefore the number of high velocity

stars which are able to affect the high velocity wings of the LOSVD is proportionately small. While the LOSVD from Template 1 might point to a detection of heavy wings, the increased difficulty of fitting the asymmetry with an axisymmetric model does not appear to result in an increase in the upper limit.

We conclude this section by discussing how the estimate of M_{BH} is affected by choice of Υ profile. We would have preferred to do this for the models with 8100 orbits; however because of the modeling time involved, we first ran a full set of models with the smaller (4500) orbit library, varying both S_Υ and M_{BH}, and then ran a subset of the larger, more time-intensive models at the value of S_Υ corresponding to the minimum found from the previous set of models. Models using 4500 orbits were therefore constructed using the Schwarzschild Υ profile for 14 different values of M_{BH} from 0.1 to $10^5 M_\odot$ and 13 values of S_Υ. The models were then fitted to the luminosity (mass) constraints, plus the GH moments obtained using Template 1. A two-dimensional χ^2 plot for this set of models is shown is Figure 11(b); the two-dimensional χ^2 plot with models that used the Carter-Sadler profile is reproduced again in Figure 11(a) for comparison. As before, the three inner most contours represent the $1\sigma, 2\sigma$ and 3σ ($\Delta\chi^2 = 2.3, 4.6, 6.1$ for DOF=2) confidence intervals respectively. In Figure 12 we plot cuts through Figures 11(a) (solid curve) and Figures 11(b) (dot-dash curve) for a fixed $M_{BH} = 10^2$. The Schwarzschild Υ profile models show a minimum at $S_\Upsilon = 0.95\pm^{0.05}_{0.08}$ (Fig. 11(b)) (as opposed to $S_\Upsilon = 1.13\pm^{0.08}_{0.1}$ in the case of the Carter-Sadler profile (Fig. 11(a)). The intercepts with the horizontal dot-dash line indicate the 1σ confidence intervals. (Note that a few additional models were run in each case to fully explore the minium). Figure 12 shows that the best fit values of S_Υ for the two models are significantly different at the 1σ level. Values of S_Υ close to the minima in Fig 12 were then chosen to construct a subset of models with 8100 orbits for all values of M_{BH}. The 1D χ^2 profiles resulting from these larger orbit libraries are shown in Figure 13 as a dot-dashed curve (the results using the Carter-Sadler profile are shown as a solid curve for comparison). The Schwarzchild profile gives $M_{BH} < 1.3 \times 10^4 M_\odot$, compared to $M_{BH} < 2.2 \times 10^4 M_\odot$ for the Carter-Sadler profile.

Finally, we note that the overall χ^2 produced by the best fit models for the two Υ profiles are virtually indistinguishable from each other (the minima differ by $\Delta\chi^2 \sim 1$), and therefore there is no reason to prefer one profile over the other. This is an indication that the 3-integral modeling problem is inherently degenerate as discussed at length in VME04.

From the discussion above we conclude that $2.2 \times 10^4 M_\odot$ represents a firm upper limit to the mass of the central black hole in NGC 205 (Table 3). Figure 14 shows the model fits to the kinematical data for $S_\Upsilon = 1.1$ (for models obtained with the Carter-Sadler profile and 8100 orbits per library) and four different black hole masses: no black hole (dot-dash line), $M_{BH} = 1.1 \times 10^3 M_\odot$ (dashed line); $M_{BH} = 2.2 \times 10^4 M_\odot$ (solid line, corresponding to the 1σ confidence upper limits for models with 8100 orbits and $\lambda = 10^{-3}$), $M_{BH} = 5 \times 10^4$ $M_\odot$ (dotted line, corresponding to the 5σ limit for the same model). The plot confirms that the two smaller values of M_{BH} produce statistically equivalent fits to the data, and that the central STIS velocity dispersion, $\sigma \sim 21$km s^{-1}, provides the strongest constraint on the upper limit on the mass of a massive central black hole.

5. IMPLICATIONS FOR BLACK HOLE SCALING RELATIONS

While the firm dynamical detection of an IBH has yet to be achieved in any galaxy, there are now two secure upper limits, in M33 (Merritt et al. 2001; Gebhardt et al. 2001) and in NGC 205 (this paper). Here we investigate the implications of these upper limits for the form of the scaling relations that have been established using SBH detections in more massive galaxies. The tightest of these relations is the $M_{BH} - \sigma$ relation as derived from central aperture dispersions (Ferrarese & Merritt 2000). This relation is plotted in Figure 15, as updated by Ferrarese & Ford (2004), using only those galaxies (25 in number) with secure dynamical detections. The solid line in Figure 15 shows the best fit regression line: $M_{BH,8} = (1.66 \pm 0.24)\sigma_{200}{}^{4.86\pm0.43}$ ($M_{BH,8} \equiv M_{BH}/10^8 M_\odot$, $\sigma_{200} \equiv \sigma/200$ km s^{-1}). Also plotted are the upper limits on M_{BH} in M33 and NGC 205. For M33, we conservatively adopt $M_{BH} < 3000$ $M_\odot$ (Merritt et al. 2001), rather than the smaller value of 1000 $M_\odot$ claimed by Gebhardt et al. (2001).

Also shown (dotted line in Figure 15) is the relation claimed by Tremaine et al. (2002), using a velocity dispersion measured by those authors within one effective radius. The difference in slopes between the two relations is barely significant in a statistical sense, but becomes critical when the relations are extrapolated to the low mass regime. The upper limits on the IBH masses in M33 and NGC 205 are both inconsistent with the shallower $M_{BH} - \sigma$ relation advocated by Tremaine et al. (2002) but not with the Ferrarese & Ford (2004) or Ferrarese & Merritt (2000) relations.

Given the importance of determining whether these upper limits on M_{BH} are consistent with the scaling relations determined at higher masses, we must address the issue of the slope. Among the differences in the way that the two groups construct the $M_{BH} - \sigma$ relation, probably the most important is sample definition. Gebhardt et al. (2000a) and Tremaine et al.(2002) adopt a less restrictive criterion than Ferrarese & Merritt (2000) in establishing the reliability of a SBH detection; in particular, they include several detection based on data which do not resolve the SBH sphere of influence (comprising roughly 30% of the claimed SBH detections based on stellar kinematics), and others (e.g. NGC 3379; Gebhardt et al. 2000b) for which the authors themselves acknowledge that a model with no SBH fits the data precisely as well as a model containing a SBH. Tremaine et al. (2002) also include SBH mass estimates which are deemed by their own authors to have systematic uncertainties that exceed the quoted errors (NGC1068, Greenhill et al. 1996; NGC 4459, NGC 4596, Sarzi et al. 2001; NGC224, Bacon et al. 2001). Empirically, the scatter in all SBH scaling relations is seen to decrease, sometimes dramatically, when detections based on galaxies which do not resolve the sphere of influence are removed from the sample (Merritt & Ferrarese 2001; Ferrarese & Ford 2004; Graham et al. 2001; Marconi & Hunt 2003). The slope is also found to increase when such detections are removed from the

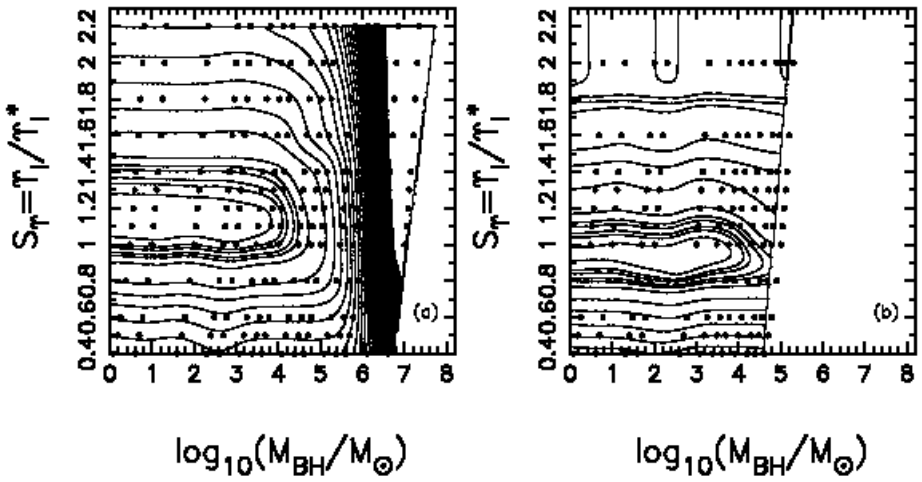

FIG. 11.— Comparion of χ^2 contour plots obtained by fitting data with libraries (of 4500 orbits) constructed with the two different Υ profiles: (a) for orbit libraries that used the Carter-Sadler profile; (b) for libraries constructed with the Schwarzschild profile.

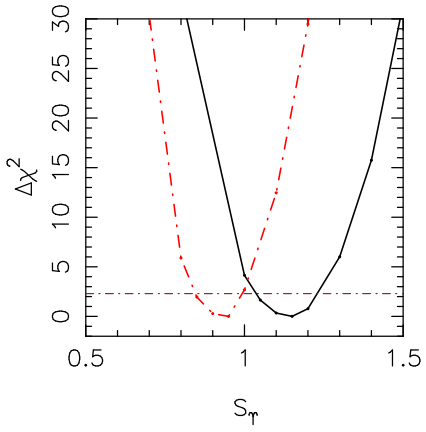

FIG. 12.— Cuts through 2Dχ^2 contour plots in Fig 11 at $M_{BH} = 10^2 M_\odot$ for the Carter-Sadler profile (solid black curve); for the Schwarzschild profile (dot-dash red curve).

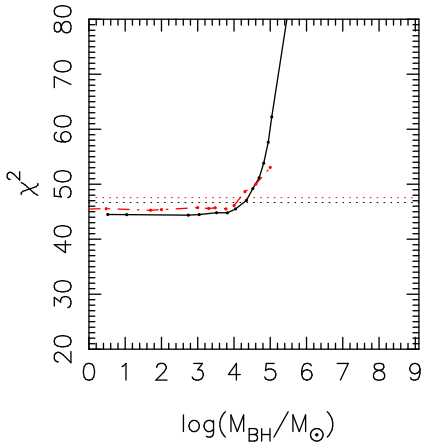

FIG. 13.— Comparion of 1D χ^2 curves at fixed values of S_Υ obtained by fitting data with libraries of 8100 orbits for libraries that used the Carter-Sadler profile (solid curve); for libraries constructed with the Schwarzschild profile (dot-dash curve).

sample (Ferrarese & Ford 2004).

Our conclusion is therefore that a steeper slope to the $M_{BH} - \sigma$ relation, such as that derived by Ferrarese & Merritt (2000) and Ferrarese & Ford (2004), is more appropriate. Therefore, the upper limits on the masses of nuclear IBH in M33 and NGC 205 are not inconsistent with the extrapolation of the $M_{BH} - \sigma$ relation to the low-mass regime. Put another way, while there is still no compelling dynamical evidence for IBHs in these galaxies, we can not yet rule out the presence of IBHs with masses similar to those predicted by the established scaling relations.

Rather than examine whether the upper limits on M_{BH} in M33 and NGC 205 are consistent with the $M_{BH} - \sigma$ relation, we can rederive that relation under the *assumption* that it applies to both galaxies, using the upper limits on M_{BH} as constraints. We apply a technique called "regression with censored data" that is now standard amongst statisticians and has been applied in a few astronomical contexts (e.g. Isobe, Feigelson & Nelson 1986). Two censored regression methods are in wide use: the EM algorithm (Dempster, Laird & Rubin 1977), a maximum likelihood method that assumes a normal distribution of the ordinate values about the best-fit line; and a modification of the EM algorithm by Buckley & James (1979), hereafter the BJ algorithm, which infers the Y-distribution from the measurements themselves and is believed to be more robust to non-normal errors. Unfortunately, neither algorithm takes into account measurement errors in either variable,[5] and for neither is there a well-accepted scheme for estimating the uncertainties in the fitted coefficients. In addition, these algorithms assume that the upper limits are precisely known.

Table 4 gives coefficients in the fit of the data in Figure 14 to

$$\log_{10} M_{BH,8} = \alpha \log_{10} \sigma_{200} + \beta. \quad (1)$$

We used the implementations of the EM and BJ algorithms provided by Isobe et al. (1986). The first line in Table 4 gives the slope (4.52 ± 0.36) and intercept when M33 and NGC 205 are excluded. The slope is slightly

[5] This was also the case for the regression algorithm used by Gebhardt et al. (2000a) in their derivation of the slope of the $M_{BH} - \sigma$ relation.

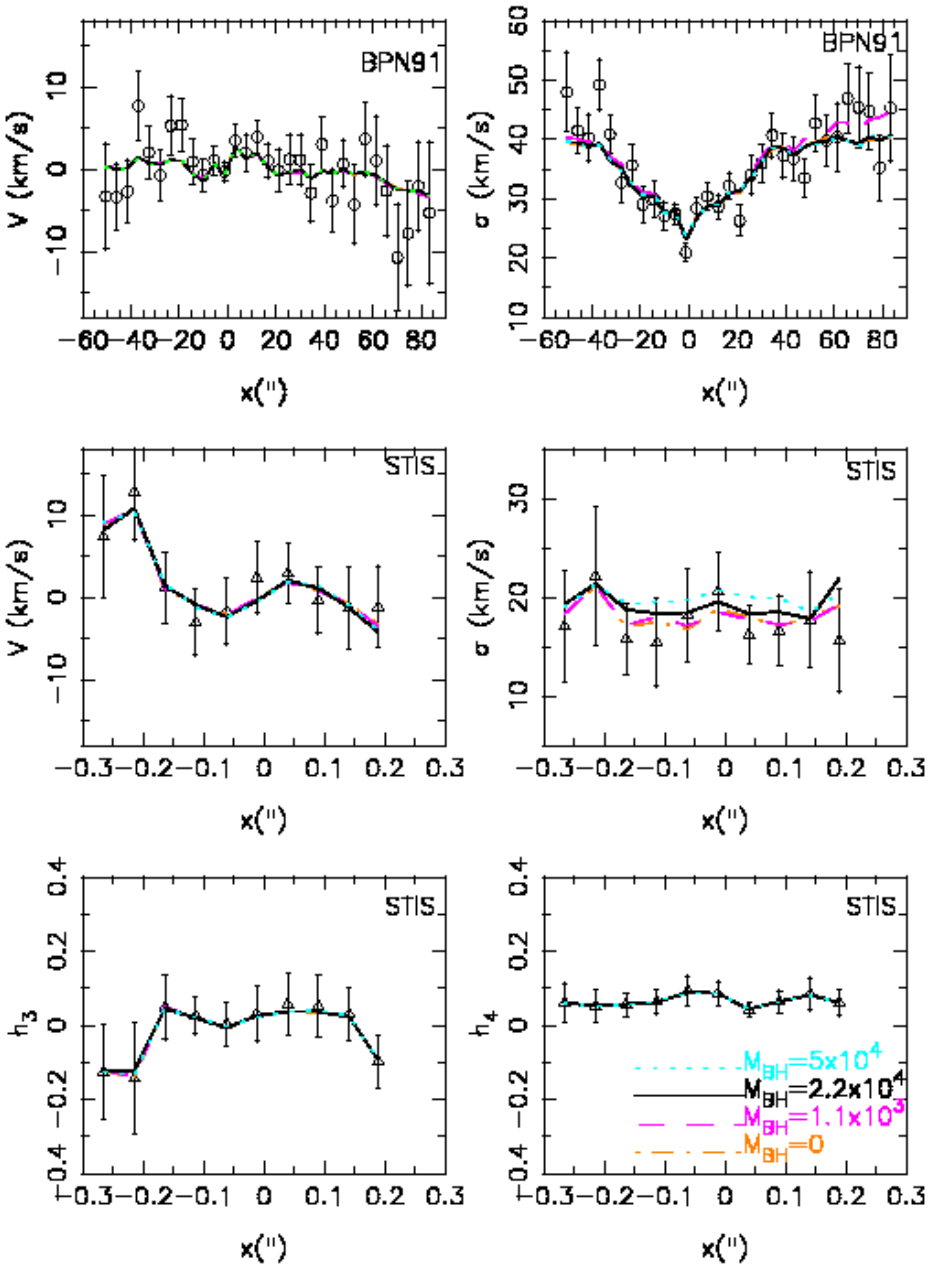

FIG. 14.— Fit to ground based data of Bender et al. (1991) (top two panels) and STIS data (bottom 4 panels) with libraries of 8100 orbits for 4 different value of M_{BH} as indicated by the labels. The solid line is the fit for the upper limit $M_{BH} = 2.2 \times 10^4 M_\odot$.

lower than the value (4.86) quoted above; the latter was derived from a regression algorithm that accounts for measurement errors (in general, ignoring measurement errors leads to spuriously low estimates of the slope). The remaining lines give the fitting parameters from the EM and BJ algorithms, respectively, under two assumptions about the upper limits on M_{BH} in M33 and NGC 205. Including the two upper limits always increases the inferred slope, to values in the range $5.2 \lesssim \alpha \lesssim 5.7$. Had we been able to include measurement errors in the censored regression algorithms, these slopes would probably have been even greater. We consider these values to be the best current estimates of the slope of the $M_{BH} - \sigma$ relation, under the assumption that *the relation extends to spheroids as faint as M33 and NGC 205.*

TABLE 4
FITS TO $\log M_{BH,8} = \alpha \log \sigma_{200} + \beta$

$M_{BH}(M33)$	$M_{BH}(NGC205)$	α	β
—	—	4.52 ± 0.36	0.22 ± 0.06
< 3000	$< 10,000$	5.48(5.43)	0.17(0.17)
< 1000	$< 10,000$	5.67(5.58)	0.16(0.17)
< 3000	$< 35,000$	5.29(5.23)	0.18(0.18)
< 1000	$< 35,000$	5.52(5.43)	0.17(0.17)

6. MORPHOLOGICAL CONSTRAINTS ON THE PRESENCE OF A MASSIVE BH IN NGC 205

The presence or absence of a massive black hole in NGC 205 might be inferred indirectly, from the observed

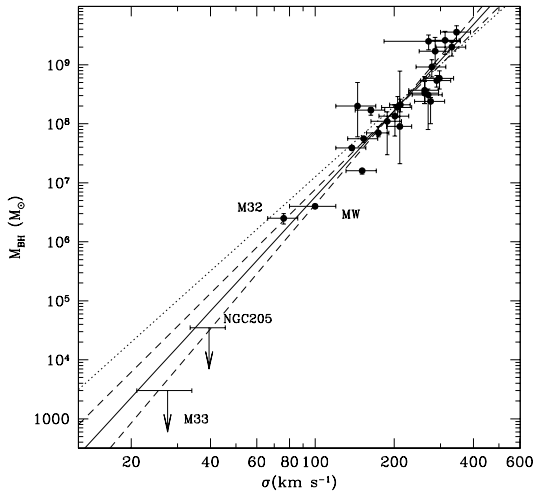

FIG. 15.— $M_{BH} - \sigma$ relation. Solid line is the best fit from Ferrarese & Ford (2004), with 1σ errors on the slope shown by the dashed line. The dotted line is the best fit from Tremaine et al. (2002). Only masses based on data which resolve the sphere of influence are plotted; the stellar velocity dispersion σ is as defined in Ferrarese & Merritt (2000).

structure of the nucleus combined with evolutionary arguments. We begin by contrasting the structure of NGC 205 with that of the other well-resolved Local Group spheroids, in M31, M32, M33, and the Milky Way (Lauer et al. 1992, 1998; Genzel et al. 2003). Each of these galaxies exhibits a steep luminosity profile, $\rho \sim r^{-\gamma}$, $1.5 \lesssim \gamma \lesssim 2$, inward of ~ 1 pc, with densities at 0.1 pc that range from $\sim 10^6 M_\odot$ pc^{-3} (M33) to $\sim 10^7 M_\odot$ pc^{-3} (M32). Only M33 and NGC 205 exhibit a core, with radius ~ 0.2 pc in both galaxies. The inferred central density of M33, assuming $M/L_v = 0.4$ in solar units, is $\sim 2 \times 10^6 M_\odot$ pc^{-3} (Lauer et al. 1998), compared with $\sim 3 \times 10^5 M_\odot$ pc^{-3} in our mass model of NGC 205. M33 and NGC 205 also have similar central kinematics: the 1D central rms velocity is $\sim 20-30$ km s^{-1} in both galaxies, compared with much higher values at the centers of the other Local Group galaxies.

The lack of a dynamical detection of a massive BH in NGC 205 also implies an upper limit to its gravitational influence radius, $r_h \lesssim 0.16$pc $M_{BH,4}\sigma_{20}^{-2}$ ($M_{BH,4} \equiv M_{BH}/10^4 4M_\odot$, $\sigma_{20} \equiv \sigma/20$ km s^{-1}). While no clear morphological signature is apparent at r_h in any of the other Local Group galaxies, even those belived to contain massive BHs, the power-law density cusps in M32 and the Milky Way are at least consistent with the $\rho \sim r^{-7/4}$ density profile that is established around a BH on a relaxation time scale T_r (Bahcall & Wolf 1976), where

$$T_r = \frac{0.34\sigma^2}{G^2 m_\star \rho \ln\Lambda} \approx 1.4 \times 10^8 \mathrm{yr} \sigma_{20}^3 \rho_5^{-1} (\ln\Lambda_{10})^{-1} \quad (2)$$

($\rho_5 \equiv \rho/10^5 M_\odot$ pc^{-3}, $\ln\Lambda_{10} \equiv \ln\Lambda/10$.) The outer radius of such a cusp is expected to be $\sim 0.2 r_h$ (Preto, Merritt & Spurzem 2004), making it unobservable in NGC 205 even if we adopt our upper limit on M_{BH}.

Figure 16 plots T_r as a function of radius in NGC 205; we also plot the time scale T_{coll} for star-star collsions,

$$T_{coll} = \left[16\sqrt{\pi} n \sigma r_\star^2 (1+\Theta)\right]^{-1} \approx 8.5 \times 10^{10} \mathrm{yr} \sigma_{20}^{-1} n_5^{-1} \Theta_{200}^{-1} \quad (3)$$

where n_5 is the stellar number density in units of 10^5 stars ($M_\odot$) per pc^3, $m_\star$ and $r_\star$ are a typical stellar mass and radius respectively, and $\Theta \equiv G m_\star/(2\sigma^2 r_\star)$. We evaluted these two time scales as functions of radius using kinematical quantities taken from our Schwarzschild solutions, setting $\sigma^2 = (\sigma_x^2 + \sigma_y^2 + \sigma_z^2)/3$, $m_\star = M_\odot$, $r_\star = R_\odot$, and $\ln\Lambda = 10$. The results were found to be almost the same whether the assumed BH mass was ~ 0 or 2.2×10^4 M$_\odot$; Figure 16 shows the results for $M_{BH} = 0$. While the stellar collision time is not directly relevant to the issues addressed in this Section, we note that T_{coll} is sufficiently long even at 0.1 pc in NGC 205 that a typical solar-type star is unlikely to have suffered a collision in its lifetime. In this respect NGC 205 is similar to other Local Group spheroids, all of which have $T_{coll}(0.1\mathrm{pc})$ of order 10^{11} yr. Hence we ignore collsions in what follows. Collisions might nevertheless have played a role in establishing the M/L gradient in NGC 205, a subject that will be discussed in more detail in a later paper.

Figure 16 shows that the relaxation time in NGC 205 is quite short, with a central value of $\sim$ a few $\times 10^7$ yr. Among the Local Group spheroids, only M33 has a comparably short central relaxation time, $T_r \approx 5 \times 10^6$ yr. The low value of T_r in M33 prompted the suggestion (Hernquist, Hut & Kormendy 1991) that the nucleus of this galaxy might have undergone core collapse. In the remainder of this Section, we discuss whether a similar case can be made for NGC 205, and whether the changes induced in the nuclear morphology of NGC 205 by core collapse would depend on the presence of a massive BH.

The case for core collapse in M33 is based on its short central relaxation time. If core collapse has *not* already occurred in M33, it would be expected to take place in a time $T_{cc} \approx 10^2 T_r(0) \approx 3 \times 10^8$ yr, with $T_r(0)$ the current central relaxation time. Unless we live at a special time, it is therefore very likely that the M33 nucleus has already undergone core collapse. The constant-density core of M33 might be a result of the binary-driven reexpansion that takes place following collapse.

This argument is not quite as strong in the case of NGC 205. We note that the exact constant of proportionality between T_{cc} and $T_r(0)$ depends on the details of the stellar distribution function, and can vary from ~ 10 to $\sim 10^3$ (Quinlan 1996). However the nuclear density profile of NGC 205 is reasonably close to the self-similar, $\rho \propto r^{-2.2}$ form of late core collapse, and the current central relaxation time is short enough that considerable evolution toward core collapse must have already occurred. In these circumstances, the constant of proportionality should be close to its asymptotic value, $T_{cc} \approx 330 T_r(0)$ (Spitzer 1987), and the current central value of T_r implies that the time remaining to core collapse (if it has not already occured) is $\sim 1.6 \times 10^{10}$ yr. This time could be shortened somewhat if the central density rises inward of the resolution limit, or if the nucleus contains a range of stellar masses (e.g. Gürkan et al. 2004). However T_{cc} is not short enough that we can conclude, as in M33, that core collapse has definitely occurred, and this makes it more difficult to draw definite conclusions about the effects of a massive BH on nuclear evolution.

If a massive BH were present at the center of NGC

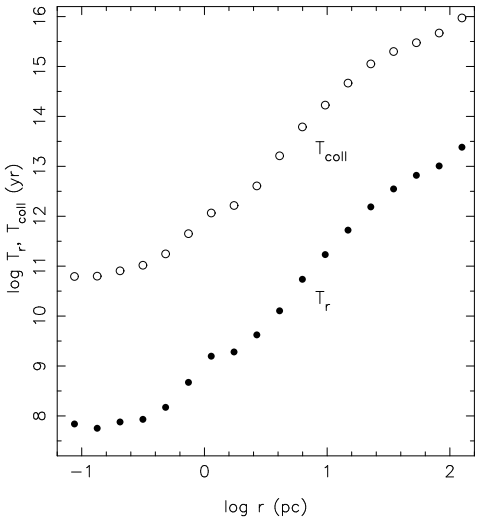

FIG. 16.— Relaxation time T_r and stellar collision time T_{coll} as functions of radius along the major axis in NGC 205, in the model solution with $M_{BH} = 0$. See text for details.

205, how would this affect the evolution toward core collapse or its subsequent effects on nuclear morphology? The theory of core collapse in the presence of a BH has not been as widely developed as the theory of core collapse in a purely stellar system, and most discussions make particular assumptions about the efficiency of accretion of gas from tidally-disrupted stars and its effect on the growth of the BH (e.g. Shapiro 1977; Murphy, Cohn & Durisen 1991; Baumgardt et al. 2004). In its early stages, core collapse around a BH is driven by the same evaporation of high-velocity stars that drives classical core collapse (Henon 1961). Collapse is eventually halted, either by binary formation, or by the input of heat due to capture or disruption of stars by the BH. The latter process is expeced to dominate the former at densities like those of the nucleus of NGC 205 (Murphy, Cohn & Durisen 1991); the core then re-expands, on a time scale of order the stellar consumption time, or $\sim T_r(r_h)$. Outside of the BH's sphere of influence, the density profile in a post-core-collapse nucleus is probably similar to that in a nucleus without a BH (e.g. Fig. 8b of Murphy et al. 1991). Significant differences in the rate of core collapse or its effects on the structure of the nucleus would only be expected if the BH were large enough that stellar capture or disruption dominated from the outset (Shapiro 1977).

We conclude that the structure and kinematics of NGC 205 do not allow us to make a definitive statement about whether or not there is morphological evidence for a central SBH. Core collapse may have occurred, but it is also possible that the core is still evolving toward collapse.

7. CONCLUSIONS

We discussed new HST ACS/HRC images and STIS spectra for the nuclear region of NGC 205, a nucleated dwarf elliptical companion of the Andromeda galaxy. The surface brightness profile derived from the $I-$band images was combined with large scale ground based data from Lee (1996) and deprojected non-parametrically to derive the 3-D luminosity density. The kinematical information (velocity, velocity dispersion and the GH h_3 and h_4 coefficients), extracted from the STIS spectra by means of a maximum penalized likeliwood algorithm, does not seem to depend significantly on the choice of stellar template. The STIS spectra are complemented at large radii with data from Bender et al. (1991). The full suite of data provides both luminosity and kinematic information up to 1.4 arcmin from the center (305 pc at the galaxy distance of 740 kpc).

In an effort to constrain the presence of a central black hole, state-of-the-art 3-integral dynamical models based on orbital superposition were constructed for a large number of the parameters $[M_{BH}, S_\Upsilon]$, where $S_\Upsilon = \Upsilon_I(r)/\Upsilon^*_I(r)$ controls the scaling of the radially variable stellar M/L ratio relative to a "nominal" value.

Several sets of models were computed and compared with the data, under different assumptions regarding the number of orbits, the value of the regularization parameter, and the radial dependence of the mass-to-light ratio. Model predictions were compared with two sets of observed kinematics, derived from the STIS data using different template spectra. We also compared the constraints imposed with and without the inclusion of the central LOSVD.

Under no set of assumptions were we able to recover a best-fit value of M_{BH} in NGC 205. The upper limit which we derive on M_{BH} is somewhat dependent on the assumptions made in the modelling, as expected based on earlier work (VME04). We found upper limits ranging from $\sim 0.8 \times 10^3 M_\odot$to $\sim 3.5 \times 10^4 M_\odot$. Even for the largest of these upper limits, the radius of influence of the black hole would not be resolved by our data, hence the failure of the modelling to produce a firm detection is not surprising. An upper limit of $2.2 \times 10^4 M_\odot$for the black hole in NGC 205 – our preferred value (§4.2) – is consistent with the extrapolation to the low-mass regime of the $M_{BH} - \sigma$ relation derived from black holes more massive than $\sim 10^6 M_\odot$.

We wish to thank the anonymous referee for the many suggestions which significantly helped in improving this manuscript. MV thanks Eric Emsellem for detailed comments on an earlier version of this paper and M.Y. Poon for assistance with extracting published ground based data from the literature. This work was supported by STScI grant GO-09448 and grants AST-0206031, AST-0420920 and AST-0437519 from the NSF and grant NNG04GJ48G from NASA.

REFERENCES

Bacon, R., Emsellem, E., Combes, F., Copin, Y., Monnet, G., & Martin, P. 2001, A&A, 371, 409
Bahcall, J. N. and Wolf, S. 1976, ApJ, 216, 883
Baumgardt, H., Hut, P., Makino, J., McMillan, S., & Portegies Zwart, S. 2003a, ApJ, 582, L21
Baumgardt, H., Makino, J., Hut, P., McMillan, S., & Portegies Zwart, S. 2003b, ApJ, 589, L25

Baumgardt, H., Makino, J., & Ebisuzaki, T. 2004, ApJ, 613, 1133
Bender, R., Paquet, A. & Nieto, J.L. 1991, A&A, 246, 349
Bica, E., Alloin, D. & Schmidt 1990 A&A, 228, 23
Bower, G. A. et al. 2001, ApJ, 550, 75
Bromley, J. M., Somerville, R. S., Fabian, A. C. 2004, MNRAS, 350, 456
Buckley, J. & James, I. 1979, Biometrika, 66, 429
Cappellari, M., Bertola, F., Burstein, D. Buson, L. M., Greggio, L. Renzini, A. 1999, ApJ, 515, 17
Cappellari, M. et al. 2002, ApJ 578, 787
Cardelli, J.A., Clayton, G.C., & Mathis, J.S. 1989, ApJ, 345, 245
Carter, D. & Sadler, E. 1990, MNRAS, 245, P12
Cattaneo, A., Haehnelt, M. G., & Rees, M. J. 1999, MNRAS, 308, 77
Condon, J.J., et al. 1998, AJ, 115, 1693
Cretton, N., de Zeeuw, P. T., van der Marel, R. P., & Rix, H.-W. 1999, ApJS, 124, 383
da Costa, G.S., & Mould, J.R. 1988, ApJ, 334, 159
Davidge, T. J. 2003, ApJ, 597, 289
Dempster, A. P., Laird, N. M., & Rubin, D. B. 1977, J. Roy. Stat. Soc. B, 39, 1
Erwin, P., Graham, A. W., & Caon, N. 2004, in "Coevolution of Black Holes and Galaxies, Carnegie Observatories Astrophysics Series Vol. 1", ed. L. C. Ho (Cambridge: Cambridge University Press), p. 264.
Fabbiano, G., Kim, D.-W., & Trinchieri, G. 1992, ApJS, 80, 531
Ferrarese, L., et al. 2000, ApJ, 529, 745
Ferrarese, L. 2002, ApJ, 578, 90
Ferrarese, L. and Merritt, D. 2000, ApJ, 539, L9
Ferrarese, L. and Ford, H. 2004, Space Science Reviews, in press
Filippenko, A. & Ho, L. 2003, ApJ, 588, L13, 2003
Fischer, P., et al. 1992, AJ, 103, 857.
Gebhardt, K. et al. 2000b, AJ, 119, 1157
Gebhardt, K. et al. 2000a, ApJ, 539, L13
Gebhardt, K., et al. 2001, AJ, 122, 2469
Gebhardt, K., Rich, R.M., & Ho, L.C. 2002, ApJ, 578, 41
Gebhardt, K. et al. 2003, ApJ 583, 92
Genzel, R., et al. 2003, ApJ, 594, 812
Gerssen, J., et al. 2002, AJ, 124, 3270
Gerssen, J., et al. 2003, AJ, 125, 376
Ghez, A.M., et al. 2003, ApJ, 586, L127
Gerhard, O. E. 1993, MNRAS, 265, 213
Graham, A.W., Erwin, P., Caon, N., & Trujillo, I. 2001, ApJ, 563, L11
Greenhill, L.J., Gwinn, C.R., Antonucci, R., & Barvainis, R. 1996, ApJ, 472, L21
Greene, J. E. & Ho, L. C. 2004, ApJ, 610, 722
Gürkan, M. A., Freitag, M., & Rasio, F. A. 2004, ApJ, 604, 632
Haehnelt, M. G., Natarajan, P., & Rees, M. J. 1998, MNRAS, 300, 817
Ho, L., Filippenko, A.V., & Sargent, W.L.W. 2003, ApJ, 583, 159
Henon, M. 1961, Ann. Ap. 24, 369
Hernquist, L., Hut, P., & Kormendy, J. 1991, Nature, 354, 376
Islam, R., Taylor, J. & Silk, J. 2003, MNRAS, 340, 647I
Isobe, T., Feigelson, E. D., & Nelson, P. I. 1986, ApJ, 306, 490
Jedrzejewski, R. I. 1987, MNRAS, 226, 747
Jones, D.H., et al. 1996, ApJ, 466, 742
Joseph, C. L. et al. 2001, ApJ, 550, 668
Kim, S.C., & Lee, M.G. 1998, JKAS, 31, 51
Kormendy, J., & Richstone, D., 1995, ARA&A, 581
Lee, M.G. 1996, AJ, 112, 1438
Lauer, T. R., et al. 1992, AJ, 104, 552
Lauer, T. R., Faber, S. M., Ajhar, E. A., Grillmair, C. J., & Scowen, P. A. 1998, AJ, 116, 2263
Maillard, J. P., Paumard, T., Stolovy, S. R., & Rigaut, F. 2004, A&A, 423, 155
Marconi, A., & Hunt, L.K. 2003, ApJ, 589, L21
McLure, R. J. & Dunlop, J. S. 2002, MNRAS, 331, 795
McNamara,B.J., Harrison,T.E., Anderson,J. 2003, ApJ., 595, 187
Merritt, D. 1997, AJ, 114, 228
Merritt, D. & Ferrarese, L. 2001a, ApJ, 547, 140
Merritt, D. & Ferrarese, L. 2001, in "The Central Kiloparsec of Starbursts and AGN: The La Palma Connection", Astron. Soc. Pac. Conf. Ser. Vol. 249, ed. J. H. Knapen, J. E. Beckman, I. Shlosman & T. J. Mahoney (ASP: Chelsea, Michigan), 335
Merritt, D., Ferrarese, L. & Joseph, C. L. 2001, Science, 293, 1116
Merritt, D., Meylan, G. & Mayor, M. 1997, AJ, 114, 1074
Miller, M.C., & Colbert, E.J.M. 2004, Int.J.Mod.Phys., 13, 1
Miller, M.C., & Hamilton, D.P. 2002, MNRAS, 330, 232
Miyoshi, M., Moran, J., Herrnstein, J., Greenhill, L., Nakai, N., Diamond, P., and Inoue, M. 1995, Nature, 373, 127
Mobasher, B., Corbin, M., & Hsu, J.-C. 2003, "HST Data Handbook", Version 3.0, (Baltimore: STScI).
Monaco, P., Salucci, P., & Danese, L. 2000, MNRAS, 311, 279
Monaco, L., Bellazzini, M., Ferraro, F. R. & Pancino, E. 2005, MNRAS, 356,1396
Murphy, B. W., Cohn, H. N., & Durisen, R. H. 1991, ApJ, 370, 60
Peterson, R.C., & Caldwell, N. 1993, AJ, 105, 1411
Pinkney, J. et al. 2003, ApJ, 596, 903
Press, W.H., Teukolsky, S.A., Vetterling, W.T. & Flannery, B.P. 1992, "Numerical Recipes in Fortran 77 - the Art of Scientific Computing" (Cambridge: Cambridge Univ.Press)
Preto, M., Merritt, D., & Spurzem, R. 2004, ApJ, 613, L109
Portegies Zwart, S.F., & McMillan,S.L.W. 2002, ApJ, 576, 899
Portegies Zwart,S.F., Baumgardt,H., Hut,P., Makino,J., & McMillan,S.L.W. 2004, Nature, 428, 724
Quinlan, G. D. 1996, NewA, 255, 270
Sarzi, M. et al. 2001, ApJ, 550, 65
Schlegel, D. J., Finkbeiner, D. P., & Davis, M. 1998, ApJ, 500, 525
Schödel, R., Ott, T., Genzel, R., Eckart, A., Mouawad, N., & Alexander, T. 2003, ApJ, 596, 1015
Schwarzschild, M. 1979, ApJ, 232, 236
Sirianni, M., et al. 2004, SPIE, 5499, 173
Shapiro, S. L. 1977, ApJ, 217, 281
Spitzer, L. 1987, "Dynamical Evolution of Globular Clusters" (Princeton: Princeton University Press)
Tremaine, S., et al. 2002, ApJ, 574, 740
Valluri, M., Merritt, D. & Emsellem, E. 2004, ApJ, 602, 66 (VME04)
van der Marel, R. P. 1994, ApJ, 432, L91
van der Marel, R. P. & Franx, M. 1993, ApJ, 407, 525
van der Marel, R. P., Cretton, N., de Zeeuw, P. T. & Rix, H. W. 1998, ApJ, 493, 613
van den Bergh, S. 1999, ARA&A, 9, 273
Verolme, E. K. et al. 2002, MNRAS, 335, 517
Wahba, G. 1990, in "Spline Models for Observational Data", CBMS-NSF Regional Conference Series in Applied Mathematics, vol. 59 (SIAM, Philadelphia), 1990